

Flexible Rechargeable Zinc-Air Batteries through Morphological Emulation of Human Hair Array

Jing Fu, Fathy Mohamed Hassan, Jingde Li, Dong Un Lee, Abdul Rahman Ghannoum, Gregory Lui, Md. Ariful Hoque, and Zhongwei Chen*

High-energy batteries are being developed to meet an ever-increasing demand for the new wave of smart-wearable technologies and wireless communications in both personal and business use. The promise of zinc-air batteries is that they have a huge weight advantage over other comparable types, providing major improvement in energy density. They owe the superior energy density mainly to their unique “half-open” system in which the zinc reacts with oxygen drawn from the air.^[1,2] A zinc-air battery can, in theory, store as much energy as 1084 Wh kg^{-1} – up to four times more than present-day lithium-ion ones can store.^[3] Zinc-air technologies have already been applied commercially in nonrechargeable miniature devices, but their attractive rechargeability was demonstrated only recently.^[4,5] A high-performance bifunctional air electrocatalysis system, designed for both oxygen reduction reaction (ORR) while discharging and oxygen evolution reaction (OER) during charging, is the key to this rechargeability.^[6] The ORR/OER bifunctional system relies not only on durable and bifunctionally active catalysts but also on design of efficient air electrode assemblies.^[7] Most attempts to improve the performance of rechargeable zinc-air batteries have tackled the problem with bifunctional electrocatalysts in the nanoscale.^[6,8] For example, nanostructured Co_3O_4 has received much attention as an effective bifunctional catalyst due to its relatively high activity and durability in alkaline solutions. Recognition the chemical coupling of Co_3O_4 nanoparticles with graphene or mildly oxidized carbon nanotubes (CNT) has led to drastically improved ORR activity of those hybrid catalysts.^[9,10] Despite all the progress of bifunctional catalysts so far, it is, in most cases, spoiled during their inefficient assembly into suitable air electrodes through physical deposition at the macroscopic scale.^[11] That is, successive layers of the nanosized catalysts are buried, making them less attractive for application in practical zinc-air batteries. Additionally, the electrode fabrication requires the use of electrochemical inactive additives, such as polymeric binders and high-surface-area conductive catalyst support.^[12] This use causes undesirable side effects on battery performance due mainly to (1) the

increased interfacial resistance caused by the insulating characteristic of polymeric binders; (2) decomposition of the ancillary additives and resultant detachment of weakly bound catalysts from the electrode surfaces. To these ends, we have turned our attention to designing a 3D nanostructured, catalyzed air electrode with a focus on improving rechargeability, energy and power density, and wider range of potential applications.

Human hair is a protein filament that grows directly from follicles beneath the skin. A hair fiber has a spinous-like structure and unique properties such as elasticity, flexibility, self-sufficiency, and light weight. Herein, inspired by the spinous structure of human hairs and their mechanism and patterns of growth, we introduced a 3D nanoarchitected rechargeable air electrode through morphological emulation of human hair array, and demonstrate its performance in a flexible solid-state zinc-air battery. This rechargeable air electrode has an array of nanoassembled hair-like catalysts vertically and directly grown on a flexible stainless-steel (SS) mesh. Each individual hair-like catalyst of the array contains a nanoassembly of 2D mesoporous Co_3O_4 nanopetals in a 1D nitrogen-doped multiwalled carbon nanotube (NCNT). Architecting the bifunctional catalyzed air electrode through the morphological emulation of human hair array possesses several advantages over the conventional physically prepared air electrodes. First, the vertically aligned NCNT directly wired to the metallic SS mesh can minimize the electrical contact resistance between the NCNT framework and the current collector (SS mesh), greatly improving the electron transfer properties of the whole electrode. This direct wiring thus completely eliminates the voltage drop that reduces battery performance due to the interface resistance between the current collector and air electrode. Second, every individual self-standing Co_3O_4 -NCNT nanoassembly on the electrode serves as the active site, significantly enhancing active material utilization for high efficiency and power generation, especially at high local current densities. In addition, the hair-like 3D nanostructure of the Co_3O_4 -NCNT nanoassembly provides intimate interfacial contact through covalent interactions between the Co_3O_4 nanopetals and the conductive NCNT, facilitating rapid charge transfer during catalytic oxygen reactions. Third, the highly porous nature of the 3D nanoarchitected electrode allows efficient diffusion of reactants (oxygen and electrolyte) through the free space among the neighboring Co_3O_4 -NCNT nanoassemblies. This efficient diffusion within the electrode guarantees a low-concentration polarization of the battery especially at high current drains.

A schematic of the hair-like array of Co_3O_4 -NCNT/SS air electrode is illustrated in **Figure 1a**. The synthesis of Co_3O_4 -NCNT/SS is based on the following three steps (Figure S1,

J. Fu, Dr. F. M. Hassan, Dr. J. Li, D. U. Lee,
A. R. Ghannoum, G. Lui,
Dr. Md. A. Hoque, Prof. Z. Chen
Department of Chemical Engineering
Waterloo Institute for Nanotechnology
Waterloo Institute for Sustainable Energy
University of Waterloo
200 University Avenue West, Waterloo ON N2L 3G1, Canada
E-mail: zhwchen@uwaterloo.ca



DOI: 10.1002/adma.201600762

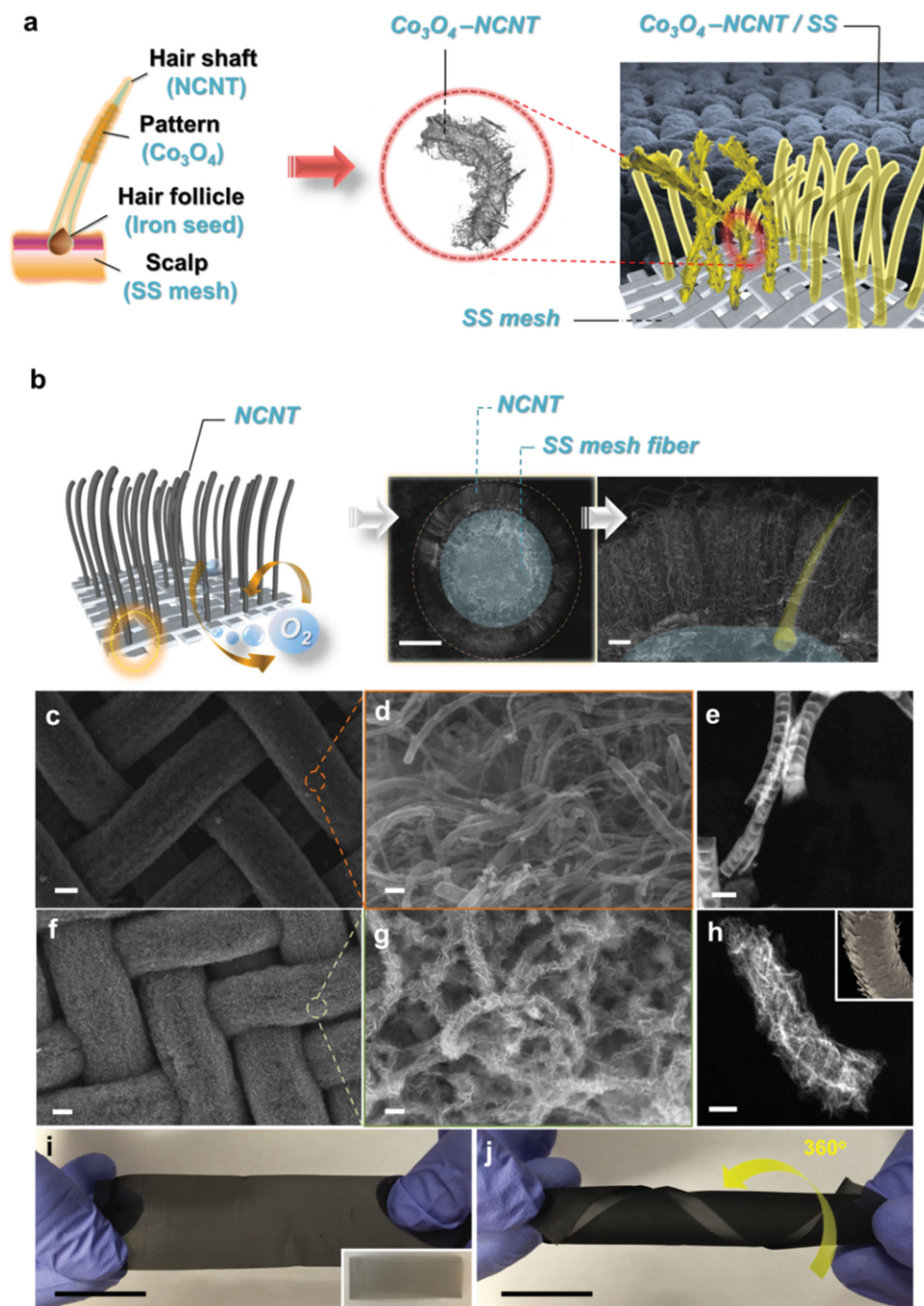


Figure 1. a) A schematic illustration of hair-like array of Co_3O_4 -NCNT/SS air electrode. b) Illustration and cross-sectional SEM images of vertically aligned NCNT framework directly grown on the surface of every individual SS mesh fibers. c, d, f, g) SEM images of the (c, d) NCNT/SS and (f, g) Co_3O_4 -NCNT/SS air electrodes. e, h) TEM images of the (e) individual NCNT and (h) Co_3O_4 -NCNT. The inset in (h) showing the petal-like (spinous) scale patterns of human hair. i, j) Digital photos of the Co_3O_4 -NCNT/SS electrode (i) without and (j) with twisting the electrode to 360° . The inset in (i) shows a bare SS mesh. Scale bar: $10\ \mu\text{m}$, $1\ \mu\text{m}$ (b), $10\ \mu\text{m}$ (c, f), $100\ \text{nm}$ (d, g), $50\ \text{nm}$ (e, h), and $2\ \text{cm}$ (i, j).

Supporting Information). First, iron oxide seeds as NCNT growth catalysts were deposited locally on the SS mesh surface by electrodeposition and subsequent calcination. Second, each individual NCNT was directly and vertically wired to the conducting surface of the SS mesh (referred to as NCNT/SS) (Figure 1b), through iron-catalyzed chemical vapor deposition (CVD). Figure S2 (Supporting Information) further reveals the

base-growth of NCNT with the iron seeds (Fe_3O_4) residing on the SS mesh substrate, similar to the process by which a hair follicle anchors each hair in skin. This approach enables direct coupling of the NCNT framework to the SS mesh without sacrificing electrical conductivity, and while retaining the beneficial characteristics of NCNT. Finally, Co_3O_4 nanopetals were uniformly distributed on the external surface of the NCNT

framework via electrodeposition and subsequent annealing, forming the array of Co_3O_4 -NCNT nanoassemblies. This vertically aligned array on the SS mesh (referred as Co_3O_4 -NCNT/SS) shares a remarkable similarity to human hair, while the porous SS mesh substrate serves as the breathable scalp skin.

As shown in Figure 1c, the bare SS mesh skeleton is densely covered with NCNT after the growth by CVD. An enlarged scanning electron microscopy (SEM) image (Figure 1d) shows that the NCNT is loosely packed, with free internal spaces. These internal spaces allow electrolyte-accessible surface areas, facilitating the electrodeposition of Co_3O_4 onto individual NCNT surfaces with a good homogeneity and distribution. The observed bamboo-like structure of NCNT with closely spaced nodes along the nanotube length (Figure 1e) can be ascribed to high-level nitrogen doping of the graphitic structure.^[13] In addition to the NCNT, the assembly of Co_3O_4 in the NCNT/SS electrode is detected in Figure 1f, where the interspace of the SS skeleton is visibly smaller than that of NCNT/SS. Figure 1g,h further shows that the Co_3O_4 was well-distributed on each individual NCNT surface, forming a unique hierarchical nanostructure similar to the human hair with petal-like (spinous) scale patterns (Figure 1h, inset). This hair-like structure of the Co_3O_4 -NCNT nanoassembly can provide intimate interfacial contact between Co_3O_4 and NCNT, favoring a low-resistance pathway for a high flux of charge transfer during ORR and OER.^[14] Additionally, the change in wettability of the air electrode after decorating the Co_3O_4 nanopetals on the NCNT is dramatic, allowing the Co_3O_4 -NCNT/SS surface to be less hydrophilic (Figure S3, Supporting Information). This effect would facilitate the diffusion of oxygen inside the electrode during the ORR. The Co_3O_4 -NCNT/SS electrode as prepared ($2 \times 8 \text{ cm}^2$)

is shown in Figure 1i, and exhibits superior flexibility even at a torsion angle of 360° (Figure 1j).

The spatial distribution of nitrogen atoms in NCNT is further identified by electron energy loss spectroscopy (EELS). As shown in Figure 2a, nitrogen atoms are well overlaid with carbon atoms along the nanotube, indicative of homogenous nitrogen doping in the bamboo-like NCNT. A high atomic nitrogen concentration of 7.96% of NCNT/SS was measured by X-ray photoelectron spectroscopy (XPS) (Figure S4a, Supporting Information). Furthermore, a high-resolution transmission electron microscopy (HRTEM) image reveals that the interlayer spacing of the outermost walls ($\approx 0.37 \text{ nm}$, blue and yellow lines in Figure 2b) is slightly larger than that of the inner graphitic walls ($\approx 0.34 \text{ nm}$, red and orange lines in Figure 2b). The smaller interlayer spacing suggests fewer nitrogen doping-induced defects in the graphitic structure of the inner walls, which could retain the electrical property of NCNT.^[10] Figure 2c displays a high-resolution N 1s XPS spectrum of the NCNT/SS. The N 1s spectrum indicates the existence of four nitrogen species, which are fitted into peaks at 398.7 eV (pyridinic N, 50.4 at%), 400.6 eV (pyrrolic N, 22.3 at%), 401.8 eV (graphitic N, 21.6 at%), and 405.3 eV (chemisorbed nitrogen oxide, 5.7 at%).^[15] The bright contrast in the high-angle annular dark field (HAADF) STEM image of the Co_3O_4 -NCNT nanoassembly and corresponding energy-dispersive X-ray spectrometry (EDX) mappings (Figure 2d) show clearly the occupancies of cobalt and oxygen atoms distributed uniformly along NCNT. XPS survey confirms the presence of Co_3O_4 , accompanied by two spin-orbit doublets at 795.87 and 780.85 eV for Co 2p_{3/2} and Co 2p_{1/2}, respectively (Figure S4b, Supporting Information). The TEM image in Figure 2e further

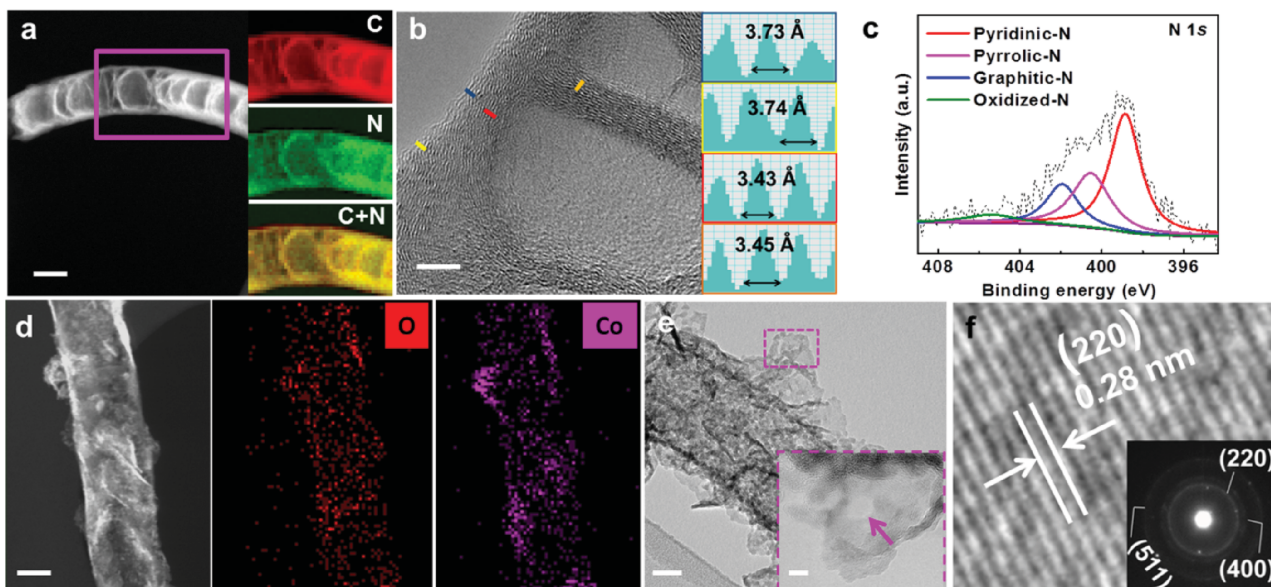


Figure 2. a) HAADF-STEM image of the NCNT and corresponding EELS mappings of carbon, nitrogen, and overlaid carbon and nitrogen atoms. b) HRTEM image of bamboo-like NCNT and corresponding line profiles along the line marked in blue, yellow, red, and orange, showing the interlayer spacing between wall layers. c) High-resolution N 1s spectrum of the NCNT/SS. d) HAADF-STEM image of the Co_3O_4 -NCNT and corresponding EDX mappings of oxygen and cobalt atoms. e) TEM image of the Co_3O_4 -NCNT nanoassembly with the inset showing the mesoporous structure of Co_3O_4 nanopetals. f) HRTEM image of the Co_3O_4 nanopetal with inset showing the SAED pattern of the major ring matching to the atomic plane with the spacing of 0.28 nm. Scale bars: 5 nm (a), 50 nm (b,d), 20 nm, 5 nm (e and inset of (e)).

reveals that each individual Co_3O_4 nanopetal is well attached in a perpendicular-like orientation to the NCNT surface, similar to the spinous structure of human hair. More importantly, these nanopetals also feature a mesoporous structure with a pore diameter of ≈ 4.5 nm (Figure 2e, inset). The mesoporosity of Co_3O_4 nanopetals observed by TEM is confirmed by Brunauer–Emmett–Teller (BET) analysis (Figure S5, Supporting Information), with the pore size distribution centered at ≈ 4.3 nm. This mesoporous structure will further enhance the electrolyte-accessible surface area and facilitate easier ion diffusion throughout the 3D nanoassembly of the electrode.^[16] The porosity of Co_3O_4 nanopetals may result from dehydration of the electrodeposited cobalt hydroxide during the mild thermal annealing process, suggestive of a phase transformation into Co_3O_4 . The lattice fringe and corresponding selected-area electron diffraction (SAED) pattern in Figure 2f reveal the spinel Co_3O_4 crystal structure of the nanopetals, which is also

confirmed by X-ray powder diffraction (XRD) (Figure S6, Supporting Information).

Figure 3a shows a typical Raman spectrum of the Co_3O_4 -NCNT/SS, exhibiting signature peaks of both NCNT and Co_3O_4 . There are two strong peaks at 1351 and 1580 cm^{-1} , corresponding to the D and G bands of NCNT, respectively. Moreover, five distinguishable peaks are identified at 686, 479, 619, 523, and 199 cm^{-1} (Figure 3a, inset). They correspond to A_{1g} , E_g , and three F_{2g} symmetric phonon modes of spinel-structured Co_3O_4 , respectively.^[17] The dominant A_{1g} peak is attributed to the Co–O breathing vibration of Co^{2+} ions in tetrahedral coordination, which is a typical characteristic of the spinel Co_3O_4 structure.^[18] Confocal Raman imaging was used to illustrate the homogeneity of the Co_3O_4 -NCNT nanoassemblies grown on the SS mesh. This spectral analysis allows for a direct visualization of the spatial variation of the electrode nanoarchitecture by integrating the intensity of characteristic spectral bands.^[19]

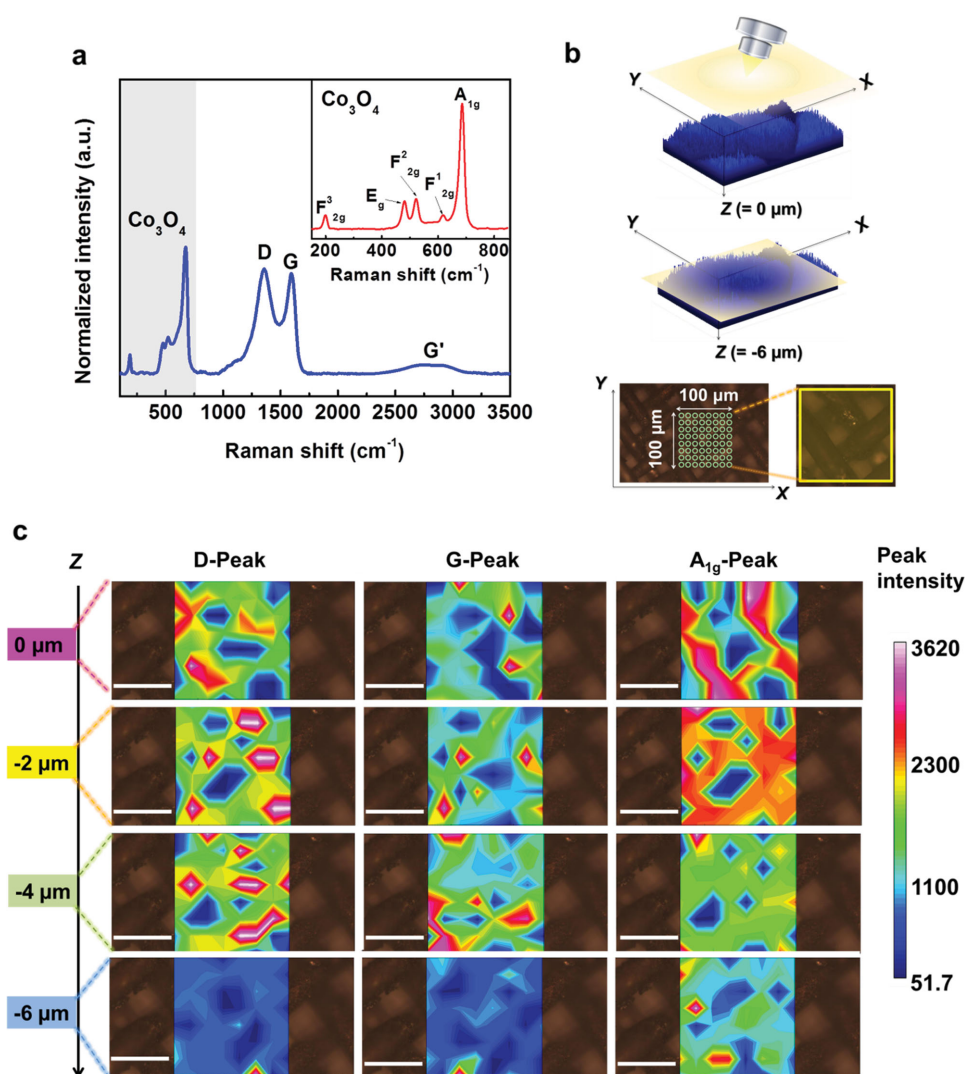


Figure 3. a) Raman spectrum of the Co_3O_4 -NCNT/SS electrode. b) Schematic of the confocal Raman set-up, with the electrode imaging-stack covering $100 \times 100 \times 6 \mu\text{m}^3$. c) Depth scanned confocal Raman imaging stacks of the Co_3O_4 -NCNT/SS electrode by integrating D peak, G peak, and A_{1g} peak, respectively. Scale bar: 50 μm (c).

Figure 3b shows schematically a xyz-coordination system of the Raman mapping of the Co_3O_4 -NCNT/SS electrode. A spot-to-spot confocal Raman mapping of the electrode assembly was acquired from 64 points covering an area of $100 \times 100 \mu\text{m}^2$ and measured as six layers in a stack for every $1.0 \mu\text{m}$ in the z-direction up to down. The overall thickness of the bare SS mesh and Co_3O_4 -NCNT/SS electrode was measured to be ≈ 56 and $\approx 70 \mu\text{m}$ (with Co_3O_4 -NCNT grown on both sides of the SS mesh), respectively. In this regard, a depth profiling with $1.0 \mu\text{m}$ resolution should effectively represent the spatial distribution of the Co_3O_4 -NCNT nanoassemblies while going down the electrode. Figure 3c displays integration maps over the D, G, and A_{1g} bands as a function of depth in the $100 \times 100 \mu\text{m}^2$ area outlined in Figure 3b. The color intensity shows the variation in vertical profile for every imaged layer with the bright regions being the highest peak intensity and the dark blue regions being pores. For the first layer ($0 \mu\text{m}$), there are the Co_3O_4 -NCNT regions identified by the strong intensities of D, G, and A_{1g} bands, corresponding to NCNT and Co_3O_4 , respectively. Additionally, the location consistency of the three characteristic profiles reveals a highly uniform distribution of the Co_3O_4 -NCNT nanoassemblies in this layer. Similarly, for integration maps of the third layer ($-2 \mu\text{m}$) and the fifth layer ($-4 \mu\text{m}$), the spatial distribution of D, G, and A_{1g} band signals do not vary significantly, where these three characteristic profiles correspond well to the SS mesh pattern. The results reveal a considerable homogeneity of the Co_3O_4 -NCNT nanoassemblies among layers of the electrode. This homogeneity is particularly evident in the seventh layer ($-6 \mu\text{m}$), which approaches the surface of the SS mesh. Compared to the less deep layers, the average intensities of both the G and D bands show noticeable decreases in the seventh layer, while the A_{1g} band retains high signal intensity. This observation indicates that each individual NCNT had its full length completely covered with Co_3O_4 nanopetals, resulting from the excellent electrical and chemical properties of NCNT. While retaining less distortion of inner walls for high conductivity, the high nitrogen doping on the outer walls provides numerous nucleation sites and thus cobalt species can be readily anchored and nucleated on the NCNT surface by electrodeposition, forming an interlaced nanopetal structure (Figure S7a, Supporting Information). To prove the role of nitrogen doping, we prepared the multiwalled CNT through the same CVD procedure followed by electrodeposition (denoted as Co_3O_4 -CNT/SS). As shown in Figure S7b,c (Supporting Information), Co_3O_4 was only deposited on the very top surface of the CNT/SS due to the weak nucleation property of the chemical inactive CNT surface.

To assess the bifunctional catalytic activity, we performed electrochemical measurements using a standard three-electrode system, in which the Co_3O_4 -NCNT/SS electrode served directly as the working electrode. The ORR and OER catalytic activities were evaluated by steady-state linear sweep voltammetry in a 0.1 M KOH solution. We found that a loading of $\approx 1.1 \text{ mg cm}^{-2}$ in the Co_3O_4 -NCNT/SS electrode yielded the optimal ORR and OER activities. For comparison, Co_3O_4 was electrodeposited on the SS mesh (denoted as Co_3O_4 /SS) by the same procedure of Co_3O_4 -NCNT/SS. Commercial state-of-the-art 20 wt% Pt/C and 20 wt% Ir/C catalysts also were deposited onto the SS mesh surface, with loading of $\approx 1.1 \text{ mg cm}^{-2}$

(denoted as Pt-C/SS and Ir-C/SS), and were measured as ORR and OER benchmarks, respectively. Three indicators were examined to evaluate the bifunctional catalytic activities: (1) the onset potential (determined as the potential at 0.1 mA cm^{-2}),^[20] (2) the specific activity (defined as the overpotential η at a current density of 10 mA cm^{-2}), and (3) the Tafel slope. The steady-state iR-compensated polarization curves of all the tested electrodes are shown in Figure 4a. The bare SS mesh shows very poor ORR activity with a negligible cathodic current density at a large overpotential (black line in Figure 4a). In contrast, Co_3O_4 /SS, NCNT/SS, and Co_3O_4 -NCNT/SS all exhibit substantial improvement in ORR activity, with their more positive shifts of the onset potential and larger diffusion-limited current densities. In particular, NCNT/SS affords an onset potential of $\approx 0.90 \text{ V}$ versus the reversible hydrogen electrode (green line in Figure 4a) and an overpotential of $\approx 0.48 \text{ V}$ at 10 mA cm^{-2} (blue bar in Figure 4b), strongly comparable to the ORR performance of Pt-C/SS, with an onset potential of $\approx 0.93 \text{ V}$ (blue line in Figure 4a) and an overpotential of $\approx 0.47 \text{ V}$ at 10 mA cm^{-2} (blue bar in Figure 4b). The nanoassembling of Co_3O_4 nanopetals on the NCNT surfaces further enhances the ORR activity of the Co_3O_4 -NCNT/SS, as reflected by the most positive onset potential ($\approx 0.95 \text{ V}$) (magenta line in Figure 4a) and the smallest overpotential ($\approx 0.44 \text{ V}$) at 10 mA cm^{-2} (blue bar in Figure 4b), outperforming those of the Pt-C/SS benchmark. Additionally, the ORR Tafel slope of Co_3O_4 -NCNT/SS (51 mV dec^{-1}) is as low as that of Pt-C/SS (52 mV dec^{-1}) (Figure 4c), revealing its superior ORR activity. On the other hand, in the anodic region the Co_3O_4 -NCNT/SS displays lower OER onset potential ($\approx 1.49 \text{ V}$) than that of SS mesh ($\approx 1.54 \text{ V}$), Co_3O_4 /SS ($\approx 1.53 \text{ V}$, red line in Figure 4a), NCNT/SS ($\approx 1.52 \text{ V}$), and Ir-C/SS benchmark ($\approx 1.51 \text{ V}$, dark yellow line in Figure 4a). By conducting OER polarization at 10 mA cm^{-2} (red bar in Figure 4b), the specific activities were found in an order of Co_3O_4 -NCNT/SS (η : 0.30 V) > Ir-C/SS (η : 0.32 V) > NCNT/SS (η : 0.34 V) > Co_3O_4 /SS (η : 0.35 V) > SS (η : 0.43 V). Furthermore, the high OER activity of Co_3O_4 -NCNT/SS is reflected by its low OER Tafel slope of 53 mV dec^{-1} (Figure 4d), strongly comparable to that of the Ir-C/SS benchmark (52 mV dec^{-1}). In addition to the high bifunctional catalytic activity, the stability of Co_3O_4 -NCNT/SS plays a crucial role in achieving a long lifecycle for rechargeable zinc-air batteries. The stability of Co_3O_4 -NCNT/SS was examined at a constant cathodic and anodic current density of 10 mA cm^{-2} in 0.1 M KOH , respectively (Figure 4e). The Co_3O_4 -NCNT/SS exhibits only small increases in the overpotential of ORR ($\approx 15 \text{ mV}$) and OER ($\approx 30 \text{ mV}$) over 7 h, whereas the ORR overpotential of Pt-C/SS and the OER overpotential of Ir-C/SS gradually increased by ≈ 60 and $\approx 51 \text{ mV}$, respectively. The slower ORR and OER activity decays of Co_3O_4 -NCNT/SS reveal its higher electrocatalytic stability than that of the Pt-C/SS and Ir-C/SS benchmarks in alkaline environment.

The outstanding ORR and OER activities as well as stability of the Co_3O_4 -NCNT/SS are likely related to its robust and flexible hair-like nanoarchitecture and synergistic effects between Co_3O_4 and NCNT. The vertically aligned array of Co_3O_4 -NCNT plays an important role in not only boosting electrocatalytic active sites, but also preventing each individual Co_3O_4 -NCNT nanoassembly from restacking and detaching from the SS mesh substrate, particularly during the OER process. To verify

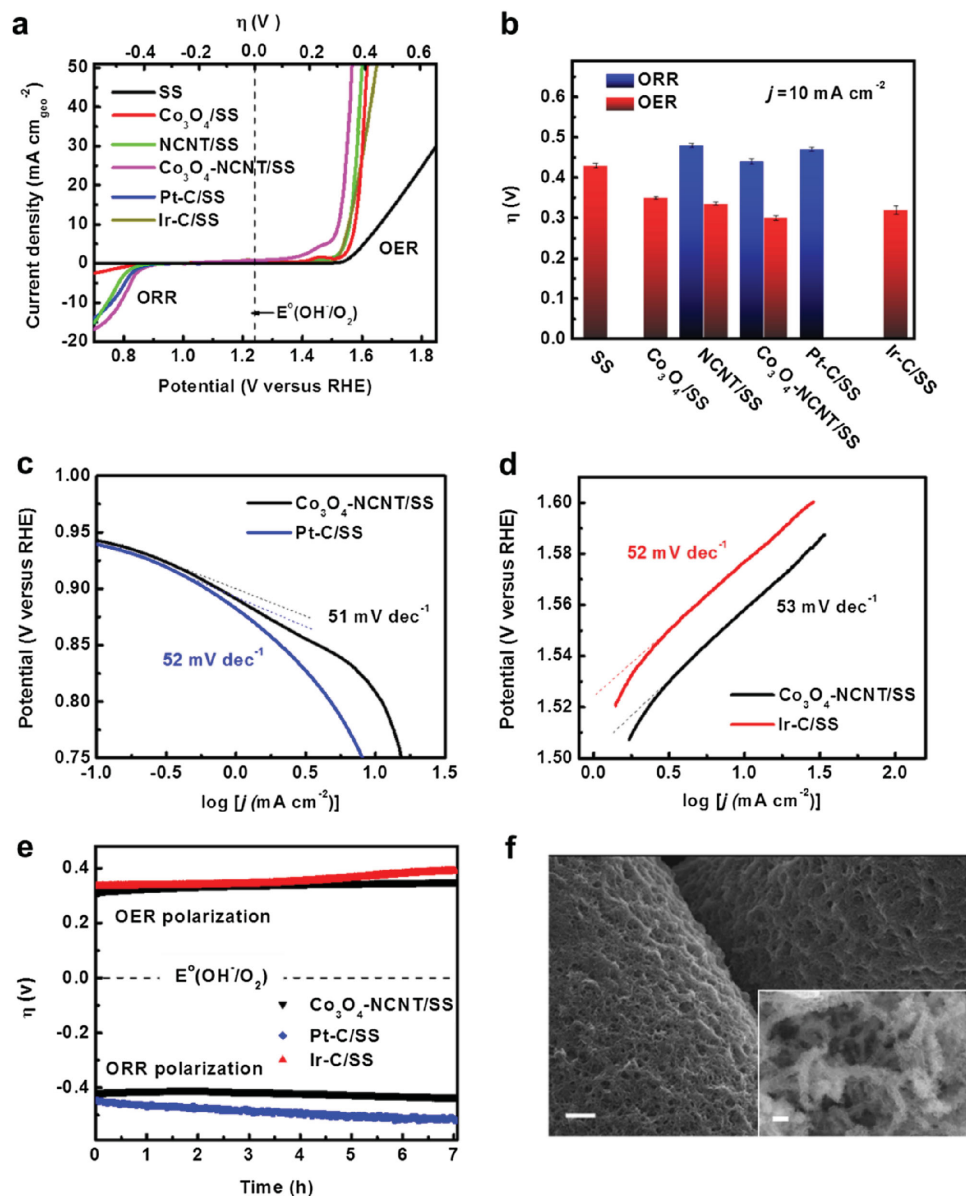


Figure 4. a) ORR and OER polarization curves and b) specific activities (at 10 mA cm^{-2}) of different air electrodes in 0.1 M KOH . c) ORR and d) OER Tafel plots of the $\text{Co}_3\text{O}_4\text{-NCNT/SS}$ electrode compared with the Pt-C/SS and Ir-C/SS benchmarks, respectively. e) Chronopotentiometric measurements of the $\text{Co}_3\text{O}_4\text{-NCNT/SS}$, Pt-C/SS, and Ir-C/SS electrodes at a constant anodic and cathodic current density of 10 mA cm^{-2} in 0.1 M KOH , respectively. f) SEM image of the $\text{Co}_3\text{O}_4\text{-NCNT/SS}$ electrode surface after the anodic chronopotentiometric measurement over 7 h. Inset: An enlarged SEM image of the $\text{Co}_3\text{O}_4\text{-NCNT/SS}$ electrode. Scale bar: $2 \mu\text{m}$ (f), 200 nm (inset of (f)).

this assumption, the surface morphologies of the $\text{Co}_3\text{O}_4\text{-NCNT/SS}$, Pt-C/SS, and Ir-C/SS electrodes after the aforementioned OER stability test were characterized. An interconnected macroporous structure was observed to form along the SS fiber surface of the $\text{Co}_3\text{O}_4\text{-NCNT/SS}$ electrode as a result of vigorous oxygen dissipation (Figure 4f), while both the Pt-C/SS and Ir-C/SS electrodes suffered from aggregation and detachment of nanoparticles (Figure S8, Supporting Information). This observation suggests that the hair-like array of the $\text{Co}_3\text{O}_4\text{-NCNT/SS}$ is robust enough to provide adequate paths for easy release of the oxygen bubbles generated during OER and to alleviate the detachment of $\text{Co}_3\text{O}_4\text{-NCNT}$ nanoassemblies from the SS mesh

surface. Only a small weight loss ($\approx 7.2\%$) of the NCNT framework was observed after the vigorous OER durability testing (Figure S9, Supporting Information).

Building on the promising electrochemical activity and stability presented above, we further demonstrated the performance of the $\text{Co}_3\text{O}_4\text{-NCNT/SS}$ air electrode using a solid-state zinc-air battery. We previously developed a thin-film battery design for flexible solid-state zinc-air application, including a free-standing zinc film, a polymer electrolyte, a catalyst-supported carbon cloth and current collectors.^[1,21] In this regard, the current collector for the air electrode is not necessary due to sufficient electrical conductivity of the $\text{Co}_3\text{O}_4\text{-NCNT/SS}$

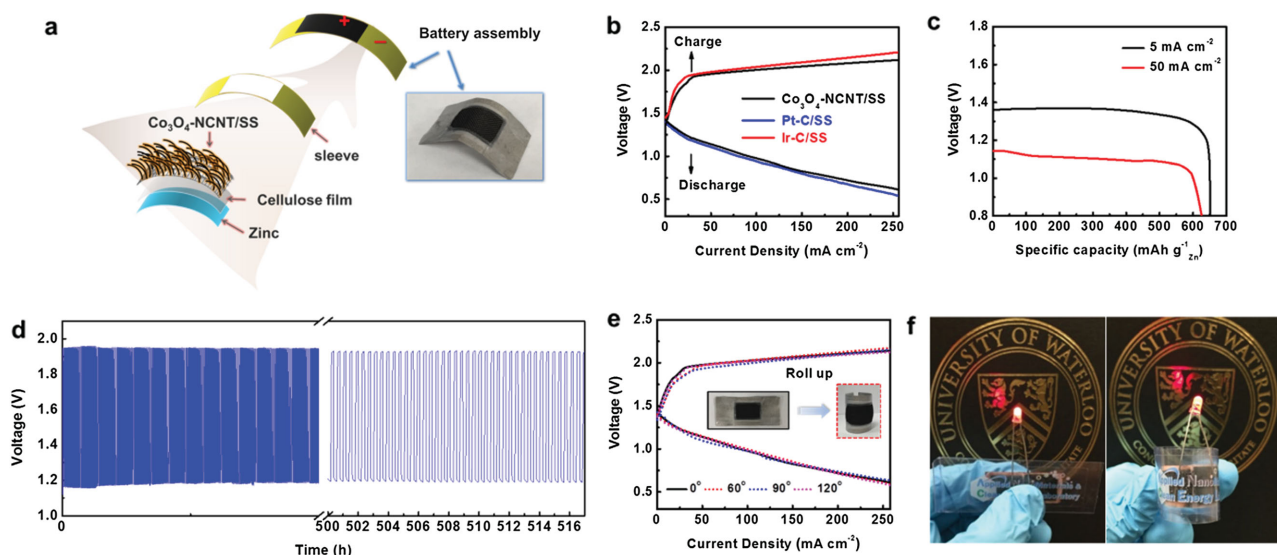


Figure 5. a) A schematic illustration of the flexible solid-state zinc-air battery assembly. b) Polarization curves of the battery using the $\text{Co}_3\text{O}_4\text{-NCNT/SS}$, Pt-C/SS , and Ir-C/SS air electrodes. c) Typical specific capacity (normalized to the mass of zinc electrode) curves of the battery using the $\text{Co}_3\text{O}_4\text{-NCNT/SS}$ air electrode at two different current densities. d) Galvanostatic charge–discharge cycling at a current density of 25 mA cm^{-2} with each cycle being 20 min. e) Polarization curves of the battery using the $\text{Co}_3\text{O}_4\text{-NCNT/SS}$ air electrode under various bending conditions. f) A demonstration of bendable device integrated with a tandem cell in series to power a LED under flat and bent conditions.

electrode. This completely eliminates the voltage drop that reduces battery performance due to the interfacial resistance between the current collector and air electrode. The porous cellulose film gelled with 6 M KOH served as the solid-state electrolyte. A thin-film battery (denoted as CoN-battery), assembled from the $\text{Co}_3\text{O}_4\text{-NCNT/SS}$ air electrode, porous cellulose film, and zinc electrode, is shown schematically in **Figure 5a** and **Figure S10a** (Supporting Information). For comparison, batteries using the Pt-C/SS and Ir-C/SS air electrodes were also fabricated through the same method and denoted as the Pt-battery and Ir-battery, respectively. **Figure 5b** displays discharge and charge polarization curves of the rechargeable battery using the $\text{Co}_3\text{O}_4\text{-NCNT/SS}$, Pt-C/SS , and Ir-C/SS air electrodes. It clearly reveals that both the discharge and charge performances of the CoN-battery (black lines in **Figure 5b**) exhibit lower overpotentials, particularly at high current densities, than those of the Pt-battery (blue line in **Figure 5b**) and Ir-battery (red line in **Figure 5b**), respectively. The performance trends are consistent with the higher ORR and OER specific activities of $\text{Co}_3\text{O}_4\text{-NCNT/SS}$ in **Figure 4a,b**. The more pronounced electrochemical performance of the $\text{Co}_3\text{O}_4\text{-NCNT}$ air electrode is due to the large amount of accessible active $\text{Co}_3\text{O}_4\text{-NCNT}$ nanoassemblies, which guarantees a higher power generation per unit area of the electrode. This is further evident from the fact that the CoN-battery yields a higher power density of 160.7 mW cm^{-2} than that of the Pt-battery (139.3 mW cm^{-2}) at 0.5 V (**Figure S10b**, Supporting Information) due to smaller interfacial and charge-transfer resistances (**Figure S10c**, Supporting Information). Additionally, the specific capacity (normalized to the mass of the zinc electrode) of the CoN-battery was ≈ 652.6 and $\approx 632.3 \text{ mAh g}^{-1}$ at a current density of 5 and 50 mA cm^{-2} , respectively, corresponding to large gravimetric energy densities of ≈ 847.6 and $\approx 802.6 \text{ Wh kg}^{-1}$ (**Figure 5c**).

To investigate the cycle stability using the $\text{Co}_3\text{O}_4\text{-NCNT/SS}$ air electrode, we performed galvanostatic discharge and charge testing on the CoN-battery at 25 mA cm^{-2} , with each cycle being 20 min. The cycling test in short interval is an excellent diagnostic tool for examining the rechargeability of the $\text{Co}_3\text{O}_4\text{-NCNT/SS}$ air electrode, while alleviating irreversible impacts from the zinc electrode.^[11] As shown in **Figure 5d**, the CoN-battery was cycled over 500 h without visible voltage losses, indicative of the excellent stability and robustness of the $\text{Co}_3\text{O}_4\text{-NCNT/SS}$ electrode. Importantly, we continued to cycle the same $\text{Co}_3\text{O}_4\text{-NCNT/SS}$ air electrode by pairing with a fresh zinc electrode, at 25 mA cm^{-2} for an additional 80 h with a much longer cycle period (10 h) (**Figure S10d**, Supporting Information). Again no significant polarization can be detected on either the discharge and charge segments. The zinc-air battery with such excellent rechargeable stability over this time-scale is strongly comparable to, or even better than, that of zinc-air batteries in trielectrode system using the conventional air electrode configurations (**Table S1**, Supporting Information).^[5,22] In addition to the outstanding cycle stability, the CoN-battery shows a great potential for flexible and wearable electronic applications. The galvanodynamic discharge and charge profiles of the CoN battery under various bending conditions are shown in **Figure 5e**. The discharge and charge potentials of the rolled-up battery remain virtually unchanged at different angles compared to these of the flat battery (0°), indicative of a robust mechanical integrity of the $\text{Co}_3\text{O}_4\text{-NCNT/SS}$ electrode under bending. The prospect of bendable application of this device is further demonstrated in **Figure 5f**. Two single CoN-batteries (size $1.0 \times 1.0 \text{ cm}^2$) were connected in series and used to light a red light-emitting diode (LED), which operates at a minimum voltage of 2.0 V .

In summary, designing the nanoarchitected catalyzed air electrode through morphologically emulating human hair could

significantly extend the limits of nanostructured catalysts based on conventional planar air electrodes. Using the $\text{Co}_3\text{O}_4\text{-NCNT/SS}$ air electrode, a practical solid-state zinc-air battery is able to deliver a high energy density of $\approx 847.6 \text{ Wh kg}^{-1}$, accompanied with excellent cycling stability over 600 h at a current density of 25 mA cm^{-2} . In addition to the pronounced electrochemical performance, the superior mechanical flexibility of the $\text{Co}_3\text{O}_4\text{-NCNT/SS}$ electrode allows its use in smart-wearable electronic applications. We believe that this advanced electrode design will give great freedom to further boost the electrochemical performance of zinc-air batteries beyond the scope of $\text{Co}_3\text{O}_4\text{-NCNT}$, through nanoengineering other heteroatom-modified CNT frameworks and transition metal oxides and chalcogenides.

Supporting Information

Supporting Information is available from the Wiley Online Library or from the author.

Acknowledgements

J.F. and F.M.H. contributed equally to this work. This research was supported by the Natural Sciences and Engineering Research Council of Canada (NSERC). TEM was obtained at the Canadian Center for Electron Microscopy (CCEM) located at McMaster University. The authors would like to thank Professor Kecheng Li at the University of New Brunswick for providing with cellulose nanofibers. The authors also thank Professor Marios Loannidis and Navid Bizmark at the University of Waterloo for helping with the water contact angle measurement.

Received: February 7, 2016

Revised: March 9, 2016

Published online: May 19, 2016

- [1] J. Fu, D. U. Lee, F. M. Hassan, L. Yang, Z. Bai, M. G. Park, Z. Chen, *Adv. Mater.* **2015**, *27*, 5617.
- [2] M. Winter, R. J. Brodd, *Chem. Rev.* **2004**, *104*, 4245.
- [3] J.-S. Lee, S. Tai Kim, R. Cao, N.-S. Choi, M. Liu, K. T. Lee, J. Cho, *Adv. Energy Mater.* **2011**, *1*, 34.
- [4] a) Y. Li, H. Dai, *Chem. Soc. Rev.* **2014**, *43*, 5257; b) B. Y. Xia, Y. Yan, N. Li, H. B. Wu, X. W. Lou, X. Wang, *Nat. Energy* **2016**, *1*, 15006.
- [5] Y. Li, M. Gong, Y. Liang, J. Feng, J.-E. Kim, H. Wang, G. Hong, B. Zhang, H. Dai, *Nat. Commun.* **2013**, *4*, 1805.
- [6] J.-I. Jung, M. Risch, S. Park, M. G. Kim, G. Nam, H.-Y. Jeong, Y. Shao-Horn, J. Cho, *Energy Environ. Sci.* **2016**, *9*, 176.
- [7] J. W. D. Ng, M. Tang, T. F. Jaramillo, *Energy Environ. Sci.* **2014**, *7*, 2017.
- [8] a) Z. Chen, A. Yu, D. Higgins, H. Li, H. Wang, Z. Chen, *Nano Lett.* **2012**, *12*, 1946; b) D. U. Lee, M. G. Park, H. W. Park, M. H. Seo, X. Wang, Z. Chen, *ChemSusChem* **2015**, *8*, 3129; c) H. W. Park, D. U. Lee, P. Zamani, M. H. Seo, L. F. Nazar, Z. Chen, *Nano Energy* **2014**, *10*, 192; d) D. U. Lee, H. W. Park, M. G. Park, V. Ismayilov, Z. Chen, *ACS Appl. Mater. Interfaces* **2015**, *7*, 902; e) Q. Li, H. Pan, D. Higgins, R. Cao, G. Zhang, H. Lv, K. Wu, J. Cho, G. Wu, *Small* **2015**, *11*, 1443; f) Y. Liang, Y. Li, H. Wang, H. Dai, *J. Am. Chem. Soc.* **2013**, *135*, 2013; g) X. Liu, M. Park, M. G. Kim, S. Gupta, X. Wang, G. Wu, J. Cho, *Nano Energy* **2016**, *20*, 315.
- [9] Y. Liang, Y. Li, H. Wang, J. Zhou, J. Wang, T. Regier, H. Dai, *Nat. Mater.* **2011**, *10*, 780.
- [10] Y. Liang, H. Wang, P. Diao, W. Chang, G. Hong, Y. Li, M. Gong, L. Xie, J. Zhou, J. Wang, T. Z. Regier, F. Wei, H. Dai, *J. Am. Chem. Soc.* **2012**, *134*, 15849.
- [11] a) Q. Sun, X. Fang, W. Weng, J. Deng, P. Chen, J. Ren, G. Guan, M. Wang, H. Peng, *Angew. Chem. Int. Ed.* **2015**, *54*, 10539; b) Y. Xu, Y. Zhang, Z. Guo, J. Ren, Y. Wang, H. Peng, *Angew. Chem. Int. Ed.* **2015**, *54*, 15390; c) D. U. Lee, J. Y. Choi, K. Feng, H. W. Park, Z. Chen, *Adv. Energy Mater.* **2014**, *4*, 1301389.
- [12] a) W. Weng, Q. Sun, Y. Zhang, S. He, Q. Wu, J. Deng, X. Fang, G. Guan, J. Ren, H. Peng, *Adv. Mater.* **2015**, *27*, 1363; b) V. Neburchilov, H. Wang, J. J. Martin, W. Qu, *J. Power Sources* **2010**, *195*, 1271.
- [13] S. Yang, G. L. Zhao, E. Khosravi, *J. Phys. Chem. C* **2010**, *114*, 3371.
- [14] Q. C. Liu, J. J. Xu, D. Xu, X.-B. Zhang, *Nat. Commun.* **2015**, *6*, 7892.
- [15] H. Liu, Y. Zhang, R. Li, X. Sun, S. Désilets, H. Abou-Rachid, M. Jaidann, L. S. Lussier, *Carbon* **2010**, *48*, 1498.
- [16] D. Yu, K. Goh, H. Wang, L. Wei, W. Jiang, Q. Zhang, L. Dai, Y. Chen, *Nat. Nano* **2014**, *9*, 555.
- [17] a) J. Yang, H. Liu, W. N. Martens, R. L. Frost, *J. Phys. Chem. C* **2010**, *114*, 111; b) R. B. Rakhi, W. Chen, D. Cha, H. N. Alshareef, *Nano Lett.* **2012**, *12*, 2559.
- [18] V. G. Hadjiev, M. N. Iliev, I. V. Vergilov, *J. Phys. C: Solid State Phys.* **1988**, *21*, L199.
- [19] K. Majzner, A. Kaczor, N. Kachamakova-Trojanowska, A. Fedorowicz, S. Chlopicki, M. Baranska, *Analyst* **2013**, *138*, 603.
- [20] S. Chen, J. Duan, M. Jaroniec, S.-Z. Qiao, *Adv. Mater.* **2014**, *26*, 2925.
- [21] J. Fu, J. Zhang, X. Song, H. Zarrin, X. Tian, J. Qiao, L. Rasen, K. Li, Z. Chen, *Energy Environ. Sci.* **2016**, *9*, 663.
- [22] J. Zhang, Z. Zhao, Z. Xia, L. Dai, *Nat. Nano* **2015**, *10*, 444.